Eur. Phys. J. D **6**, 255–267 (1999)

THE EUROPEAN PHYSICAL JOURNAL D

EDP Sciences

Tight-binding studies of surface effects on electronic structure of CdSe nanocrystals: the role of organic ligands, surface reconstruction, and inorganic capping shells

S. Pokrant[a] and K.B. Whaley[b]

Department of Chemistry, University of California at Berkeley, Berkeley, CA 94720, USA

Received 21 September 1998 / Received in final form: 15 December 1998

Abstract. We utilize a tight-binding model to study the effects of surface structure on electronic properties of CdSe clusters. The model takes into account experimental information about structure and shape of the nanocrystals, as well as the nature and distribution of capping ligands. The effects of both organic capping ligands and inorganic capping shells on the densities of states (DOS) and on the single-particle absorption spectra of the clusters are calculated for various cluster shapes and sizes, and are compared to results for clusters with truncated surfaces. For organic capping ligands, the effect of ligand hybridization is investigated and a simple model of surface reconstruction is developed. Both ligand hybridization and surface reconstruction are seen to have a major influence on the band edge electronic and optical properties. Inorganic capping shells give rise to differential localization of valence and conduction band edge states, with the hole primarily confined to the core region and the electron more evenly distributed over both core and shell.

PACS. 71.24.+q Electronic structure of clusters and nanoparticles 71.55.Gs II-VI semiconductors 73.20.Dx Electron states in low-dimensional structures (superlattices, quantum well structures and multilayers)

1 Introduction

The electronic and optical properties of semiconductor nanocrystals have generated considerable interest in recent years because of the role played by quantum confinement and the consequent potential which they offer for size-tunable nanoscale devices [1]. The general features of quantum confinement can be qualitatively understood in terms of ideally confined electrons, *i.e.*, employing hard wall barriers [2–4]. This has lent itself readily to the use of effective mass approximations (EMA) in which the only atomic level input is the bulk band dispersions at $k = 0$, and attention focuses on modification of the electron envelope functions induced by the confinement [5]. Incorporation of the valence band degeneracy via the multiband $k \cdot p$ method, and perturbative analysis of spin-orbit, shape and crystal field effects has allowed some analysis of fine structure effects on the band-edge-dominated optical properties to be made within EMA [6,7].

In experimental realizations, nanocrystals are formed by kinetically controlled precipitation, and are terminated with capping ligands which provide stabilization of the otherwise reactive dangling orbitals of surface atoms [8]. The extent to which the molecular nature of the surface may affect the electronic properties is not well understood. Deep trap states resulting from unsaturated surface species are well known in luminescence studies [9,10], and femtosecond time transient absorption studies indicate both electrons and holes can be surface trapped [11, 12]. However, both absorption bands and the band edge luminescence appear to be independent of surface preparation [13], and the Stokes shifts between absorption and luminescence peaks now appear to be largely consistent with excitonic fine structure [7], rather than with surface trapping as was originally proposed [9,14–18].

While a complete experimental understanding of the nature and quantitative role of surface effects is not yet at hand, it is nevertheless clear that the surface may in some instances play a significant role. Phenomenological finite surface barrier potentials have been employed within EMA to examine effects of surface polarization [19], but a microscopic understanding of features such as surface trap states requires the incorporation of atomic details. This is one motivation for developing a microscopic theoretical description of nanocrystals taking the atomic structure explicitly into account. Increasing theoretical effort has recently been invested in development of tight-binding [20–23,27–32], pseudopotential [33, 34], and density functional [35,36] methodologies for the electronic structure of nanocrystals. With such atomistic

[a] *Present address*: Department of Physical Chemistry, University of Bonn, Wegelerstrasse 12, 53115 Bonn, Germany.
[b] e-mail: whaley@holmium.cchem.berkeley.edu

calculations, a more realistic description of both the nanocrystal surface and interior now becomes possible. To date however, theoretical analysis of how the surface of nanocrystals can influence their electronic properties has been minimal, and restricted primarily to ideal, unreconstructed surfaces. The dangling surface orbitals have generally either been artificially removed (the "truncated" surface), or else saturated by species chosen to sweep surface states out of the band gap region. In a previous tight-binding study of the surfaces of unreconstructed CdSe nanocrystals [23], we showed that saturation with oxygen ligands very effectively removes Cd dangling orbitals from the band gap region, but is relatively ineffective at removing Se dangling orbitals, implying that electron traps would be removed but that some hole traps would remain when capping by oxygen-coordinating ligands. Oxygen-coordinating ligands are the most commonly used capping species, and therefore this result is of relevance to most of the experimentally studied CdSe nanocrystals. The lack of passivation of surface Se atoms when such ligands are used was confirmed by experimental studies of the surface structure for CdSe nanocrystals capped with ligands such as tri-*n*-octylphosphine oxide (TOPO) using NMR [24] and XPS [25]. A recent study for nanocrystals capped by sulphur-coordinating ligands using EXAFS and other analytical methods [26] show similar behavior, *i.e.*, the presence of Se dangling orbitals which can act as hole traps.

In this paper we now provide a more detailed analysis of the role of the surface, with a realistic study of CdSe nanocrystals which incorporates the experimentally observed shapes and lattice structures, and which also investigates for the first time the effects of variable capping ligand hybridization and of surface reconstruction. In addition, we also examine the effect of capping by layers of a second semiconductor, using a simple core/shell tight-binding model for a CdSe nanocrystal coated with several layers of CdS to form a zero-dimensional (0D) analog of a two-dimensional (2D) semiconductor heterostructure.

The methodology used here is based on the tight-binding method, which provides a useful atomistic approach to the electronic structure of semiconductor nanocrystals. It allows for an atom-by-atom construction of the surface, while at the same time taking advantage of the periodicity characterizing the interior of the nanocrystal. In empirical tight-binding, the parameters for the crystalline interior can be taken from the bulk crystal. In the context of nanocrystals, tight-binding provides a convenient empirical or semiempirical method which allows a much more detailed analysis of the electronic wave functions than EMA and its modifications, and which also allows study of clusters ranging in size from a few tens of atoms to 10^6 atoms within a consistent theoretical framework. More *ab initio* approaches such as density functional theory are now undergoing rapid development, but for systems such as CdSe are currently still limited by size to a few tens of atoms [37]. Since here our aims are to examine the effect of *large* changes in shape and surface termination on the electronic and optical properties of CdSe clusters containing a few hundred atoms, where about half of these might be surface atoms, the time-independent, direct diagonalization tight-binding method is quite appropriate here. We focus on CdSe nanoclusters, because these are experimentally the most well characterized, both in terms of their electronic structure and in terms of structural and chemical details of their surfaces. CdSe nanocrystals have been characterized by their optical properties [9,10,13,17,18,38–49], by X-ray diffraction [50,51], X-ray photoelectron spectroscopy [25], dielectric dispersion [52], nuclear magnetic resonance [24] and transmission electron microscopy measurements [53–55]. Previous theoretical studies of CdSe nanocrystals with sizes greater than 10^2 atoms have concentrated on analysis of size dependence of excitonic effects for idealized cluster shapes and surface terminations, using tight-binding [22, 23], pseudopotential [34], and multiband $k \cdot p$ methods [6, 56]. However theoretical studies have not addressed large deviations from spherical shape, nor the effects of a microscopic realistic description of the surface.

The remainder of the paper is structured as follows. In Section 2 we outline our basic tight-binding model for CdSe nanocrystals with organic capping ligands and describe the extension to deal with inorganically capped core/shell nanocrystals. Section 3 provides a summary of results for truncated nanocrystals which act as a reference, demonstrating the different roles of nanocrystal shape and size on the electronic properties. More detailed analysis of the size dependence for such reference systems can be found in reference [65]. In Section 4 we investigate the effect of ligand hybridization and surface reconstruction on organically capped CdSe nanocrystals. Section 5 examines the consequences for the electronic structure of capping the nanocrystal with epitaxially grown layers of a second semiconductor material (CdS), and Section 6 provides a brief summary.

2 Tight-binding model

Our approach is based on the use of empirical tight-binding models for the bulk semiconductors. The simplest version of an empirical tight-binding model is obtained by fitting merely the lowest conduction band and highest valence bands in the vicinity of the Γ point [32]. We employ the more extensive empirical parameterizations which are designed to reproduce the bulk band structure over a selected energy range. Spin-orbit coupling and crystal field effects are not included in the calculations presented here. The parameters we use for CdSe are derived from the empirical parameters obtained by Lippens and Lannoo for bulk CdSe in the zinc-blende structure, assuming nearest-neighbor interactions only [21]. Zinc-blende and wurtzite structures have the same tetrahedral nearest-neighbor environment, so one can apply the same set of nearest-neighbor parameters to both structures [57]. The parameter set is transformed from the Cartesian basis of reference [21] to the sp_3s^* basis of Vogl and co-workers [58] (four sp_3 hybrid orbitals, and one s^* orbital simulating the neglected d orbitals). The resulting hybridized parameter

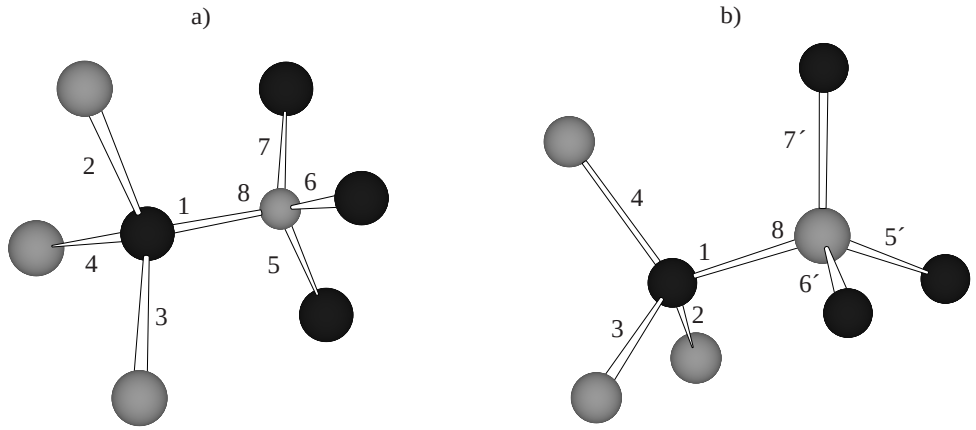

Fig. 1. (a) Staggered and (b) eclipsed conformations of nearest-neighbor anion (Se) and cation (Cd) in the wurtzite lattice. The eclipsed conformation is found along the c-axis, the staggered conformation in all other directions. Black spheres represent Se, light grey spheres Cd. The numbers label the bond-directed sp_3 orbitals used to transform the Cartesian tight-binding parameters to the sp_3s^* basis for the wurtzite structure (Tab. 1).

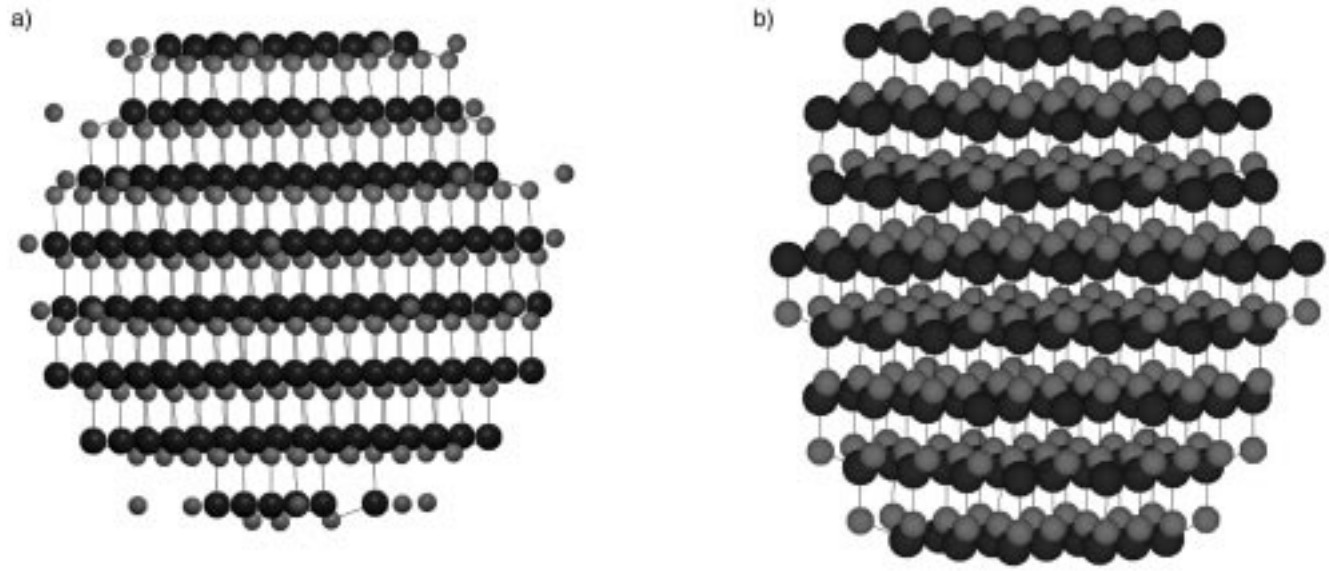

Fig. 2. (a) Side view of the 393 cluster with 30 ligands attached. Black spheres represent the Se atoms, grey spheres denote Cd. Small dark atoms on the outside of the cluster which are not connected by bonds with the interior represent the oxygen atoms of the TOPO ligands. (b) Side view of the 384 cluster without ligands.

set differs from the corresponding sp_3s^* parameter set for the zinc blende structure because of the different packing of adjacent tetrahedral units in the two structures. In zinc blende the tetrahedra are staggered in all four directions, while in wurtzite they are eclipsed along the c-axis and staggered in the remaining three directions [60]. The non-bonding interactions between orbitals on adjacent anion and cation are different in the eclipsed and staggered conformations. Figure 1 illustrates the relationship between directed sp_3 orbitals of nearest-neighbor anion and cation for both conformations, and the corresponding conversion from Cartesian to wurtzite bond-directed parameters in the sp_3s^* basis is given in Table 1. The resulting band structure for wurtzite CdSe is shown in reference [65].

In this work we vary size, shape and the surface composition, taking into account all of the available experimental data on these features. Thus all clusters modeled here show C_{3v}-symmetry (Figs. 2a and b) and are slightly prolate, with a mass distribution of approximately 1.1 : 1 : 1 along the $z : x : y$-axes, where the z-axis is defined along the bulk crystal c-axis [53,55]. This corresponds to an ellipticity $\mu = c_0/b_0 - 1 = 0.049$, where the long axis is defined as having length c_0, and the two short axes as having length b_0 [65]. We also investigate the effect of a severe change in shape, considering a highly prolate cluster with $\mu = 0.26$.

Our investigations of ligand hybridization and surface reconstruction of nanocrystals capped by organic ligands focus on capping by the commonly used TOPO ligand.

Table 1. Transformation of nearest-neighbor tight-binding parameters from Cartesian to the bond-directed sp_3s^* basis for the wurtzite lattice. The parameters in column three are related to those of reference [21] by the relations $E_{\gamma i} \equiv E(\gamma i)$ and $V_{\gamma,\gamma'} \equiv \frac{1}{4}V(\gamma a, \gamma' c)$, $a \equiv$ anion, $c \equiv$ cation, with γ denoting Cartesian orbital type. We define $V_{\gamma\gamma'}$ such that the anion always appears first, and make use of the well-known sign change between corresponding V's for $\gamma\gamma' \equiv sp$ or ps [59].

α_1	$\langle\phi_1\|H\|\phi_1\rangle$	$\frac{1}{4}(E_{sa} + 3E_{pa})$
β_1	$\langle\phi_8\|H\|\phi_8\rangle$	$\frac{1}{4}(E_{sc} + 3E_{pc})$
α_2	$\langle\phi_1\|H\|\phi_2\rangle$	$\frac{1}{4}(E_{sa} - E_{pa})$
β_2	$\langle\phi_7\|H\|\phi_8\rangle$	$\frac{1}{4}(E_{sc} - E_{pc})$
$\alpha_3 = \beta_3$	$\langle\phi_1\|H\|\phi_8\rangle$	$\frac{1}{4}(V_{ss} - 3V_{xx} - 6V_{xy} - 3V_{sp} + 3V_{ps})$
α_4	$\langle\phi_2\|H\|\phi_8\rangle$	$\frac{1}{4}(V_{ss} + V_{xx} + 2V_{xy} - 3V_{sp} - V_{ps})$
β_4	$\langle\phi_1\|H\|\phi_5\rangle$	$\frac{1}{4}(V_{ss} + V_{xx} + 2V_{xy} + V_{sp} + 3V_{ps})$
α_5	$\langle\phi_2\|H\|\phi_5\rangle$	$\frac{1}{4}(V_{ss} + V_{xx} - 2V_{xy} + V_{sp} - V_{ps})$
α_6	$\langle\phi_2\|H\|\phi_7\rangle$	$\frac{1}{4}(V_{ss} - 3V_{xx} + 2V_{xy} + V_{sp} - V_{ps})$
γ_1	$\langle s^*a\|H\|s^*a\rangle$	E_{s^*a}
γ_2	$\langle s^*c\|H\|s^*c\rangle$	E_{s^*c}
γ_3	$\langle s^*a\|H\|\phi_8\rangle$	$-\frac{3}{2}V_{s^*p}$
γ_4	$\langle s^*a\|H\|\phi_5\rangle$	$\frac{1}{2}V_{s^*p}$
γ_5	$\langle s^*c\|H\|\phi_1\rangle$	$-\frac{3}{2}V_{ps^*}$
γ_6	$\langle s^*c\|H\|\phi_2\rangle$	$\frac{1}{2}V_{ps^*}$
α'_5	$\langle\phi_2\|H\|\phi_{6'}\rangle$	$\frac{1}{4}(V_{ss} - \frac{5}{3}V_{xx} + \frac{2}{3}V_{xy} + V_{sp} - V_{ps})$
α'_6	$\langle\phi_2\|H\|\phi_{5'}\rangle$	$\frac{1}{4}(V_{ss} + \frac{7}{3}V_{xx} - \frac{10}{3}V_{xy} + V_{sp} - V_{ps})$

We use oxygen atoms bonded to the surface Cd to represent the nanocrystal-ligand bonding. The Se atoms are not saturated, for the reasons discussed above. The O-Cd interaction is described with the same set of extended Hückel parameters used in reference [23]. Whereas in that work we assumed a fixed, sp_2 hybridization for the surface-attached oxygen atom, we now examine the effects of variable hybridization. The bonding in adducts of phosphine oxides with metal atoms is a complex subject. A simple dative bond would result in sp_2 hybridization, illustrated for Cd in Figure 3. However the P-O bond length is usually increased in these adducts [61,62], consistent with a metal-oxygen σ bond with a greater degree of electron donation to Cd, stabilized by a resonance structure with positive charge on P [63]. In the extreme case this would result in an sp_3 hybridization for the oxygen atom, Figure 3. Infrared spectroscopic measurements for TOPO attached to CdSe show the decreased P-O stretch frequency characteristic of such a P-O bond length increase [25]. Complicating this picture, however, is that fact that most metal-O-P bond angles lie between 120° and 180°, suggesting some additional π character to the complexation and therefore introduction of resonance structures with sp character [62, 64]. This would also increase the extent of electron donation to the metal. We examine here the effects of the two hybridization limits for pure dative bonding, *i.e.*, sp_2 and sp_3. This allows us to vary the strength of binding to

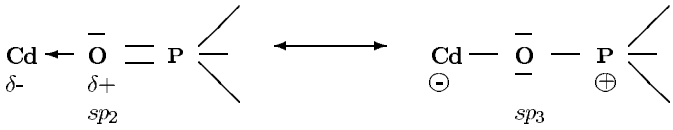

Fig. 3. Two possible resonance structures for the Cd-O-P bond, resulting in different bonding strengths.

the ligand within a simple bonding framework consistent with the use of extended Hückel parameters. The Cd-O tight-binding parameters in the sp_2 and sp_3 hybridizations are obtained by transformation of the Cartesian parameters of reference [23]. The subsequent modification of these surface-ligand tight-binding parameters upon surface reconstruction is described in Section 4.

To investigate the effects of capping by shells of a different semiconductor, we consider clusters consisting of a CdSe core surrounded by several layers of epitaxially grown CdS. The lattice constants of CdS are very similar to those of CdSe, resulting in a relatively small change in the interatomic distance, from 2.632 Å in CdSe to 2.532 Å in CdS. Experimental observations also indicate that very few stacking faults are found at the interface [78], so that both core and shell can be assumed to have the ideal bulk structure. Because of the lattice mismatch, there may nevertheless exist some strain between core and shell. While there is some evidence for this from X-ray diffraction, it does not appear to affect the electronic properties in any obvious manner [78]. Thus we neglect stress and strain at the interface here and use the CdSe bulk tight-binding parameters without any scaling for modified lattice spacings at the interface. The bulk CdSe interatomic spacings are then replaced by the bulk CdS interatomic spacings in the shell region. For CdS we use the empirical parameters of reference [20] and also transform these from the Cartesian basis to the bond-directed wurtzite basis, according to the formulae given in Table 1.

These core/shell nanostructures can be viewed as zero-dimensional (0D) heterostructures. In order to combine the CdSe and CdS empirical parameter sets to represent a heterojunction, we have to account for the band off-sets between the two materials. In bulk, 2D CdSe/CdS superlattices form a type-II heterostructure in which the bands are staggered, with both the conduction band mimimum and the valence band maximum lying lower in energy than in CdSe [66,67]. The resulting band off-sets are not automatically incorporated in our empirically derived tight-binding parameter sets, which are both constructed according to the usual convention with the zero of energy set to the top of the valence band. A further complication is that while the "indirect" gap from the CdSe valence band to the CdS conduction band has been measured [66], the individual band off-sets are not precisely known for CdSe/CdS. Therefore we modify here the CdSe/CdS tight-binding parameterization for the core/shell crystallites such that the main features of the bulk type-II heterostructure are preserved, but without guaranteeing quantitative accuracy in the band off-sets. Our modification is based on the requirement that Cd,

Table 2. On-site parameters for CdS, CdSe and CdS/CdSe core shell particles in the Cartesian basis.

	CdSe[a]		CdS[b]		CdS core/shell	
	Cd	Se	Cd	S	Cd	S
$\langle s\|H\|s\rangle$	0.03 eV	−9.63 eV	1.83 eV	−11.53 eV	0.03 eV	−12.89 eV
$\langle p\|H\|p\rangle$	4.73 eV	1.47 eV	5.87 eV	0.53 eV	4.73 eV	−0.83 eV
$\langle s^*\|H\|s^*\rangle$	5.72 eV	7.53 eV	6.87 eV	7.13 eV	5.72 eV	5.77 eV

[a] = reference [21], [b] = reference [20].

as the common cation at the interface, should have identical energies in a consistent parameterization. We therefore shift the CdS parameter scale for the shell region such that the on-site Cd energies match those in the core region, while the on-site S energies are linearly shifted by 1.36 eV. Because the cation self-energy differences are different for each orbital type, it is not possible to use a single shift for the cations. The single anion shift minimizes the linear differences between the self-energy parameters for the Cd atoms in CdS and in CdSe, and thus represents a weighted average of the variable cation shift. In practice, the resulting electronic structure is insensitive to the use of other fit criteria, such as the square of the residuals for the Cd self-energy differences. Calculation of the bulk band structure resulting from these modified parameters confirms that the CdS band structure is indeed shifted downward, with a slight accompanying distortion in the band dispersions and a decrease in the band gap. The valence band maximum is shifted down by about 1.3 eV, in reasonable agreement with the simple estimate of valence band-offset of 0.77 eV obtained from from covalent and polar energies [68]. The conduction band minimum moves down by 1.7 eV, resulting in a reduction in the CdS band gap from 2.5 eV to 2.1 eV. However the gap remains larger than that for CdSe (1.9 eV) and thus the characteristic of a core/shell structure with the larger band gap material in the shell region is preserved by the transformation. The combination of these CdSe and modified CdS parameter sets, therefore, correctly predicts a CdSe/CdS type-II bulk heterostructure, with a staggered band lineup, summarized in Figure 4. The original CdS and CdSe self-energies are listed together with the shifted parameter set for the CdS shell region in Table 2.

To quantify the opto-electronic properties of the clusters we use density of states (DOS) and single-particle absorption spectra. The DOS are obtained by summing the number of eigenstates in an energy range of 0.05 eV, where the eigenstates are obtained by direct diagonalization of the tight-binding Hamiltonian. The absorption spectrum for CdSe nanocrystals is computed in the single-particle approximation, *i.e.*, ignoring excitonic effects. The single-particle eigenfunctions are expanded in terms of atomic orbitals

$$|\chi_l\rangle = \sum_S \sum_j c^l_{Sj} |Sj\rangle \,, \tag{1}$$

with S denoting the atom site, and j the orbital index. The transition dipole moment in the x-direction between

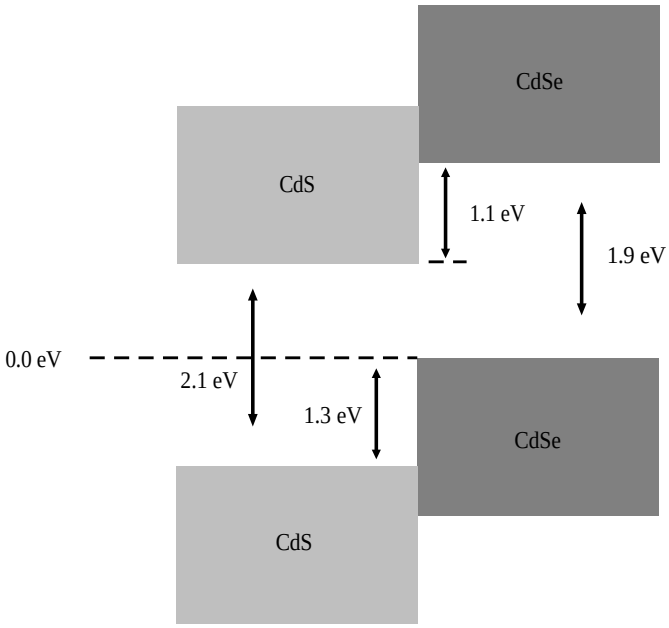

Fig. 4. Bulk band off-sets for a planar CdSe/CdS heterojunction derived from the current tight-binding model.

the eigenfunctions $|\chi_l\rangle$ and $|\chi_m\rangle$ is then given by

$$\langle \chi_l|\hat{x}|\chi_m\rangle = \sum_{SS'} \sum_{jj'} \langle Sj|\hat{x}|S'j'\rangle (c^l_{Sj})^* c^m_{S'j'}. \tag{2}$$

Since the dipole transition matrix elements between different sites are translationally invariant under the lattice translations, transforming to local coordinate frames centered on the atom sites S allows equation (2) to be rewritten as

$$\begin{aligned}\langle \chi_l|\hat{x}|\chi_m\rangle &= \sum_S \sum_{jj'} \langle j|\hat{x}|j'\rangle (c^l_{Sj})^* c^m_{Sj'} \\ &+ \sum_S \sum_n \sum_{jj'} \langle \mathbf{0}j|\hat{x}|\Delta_n j'\rangle (c^l_{Sj})^* c^m_{nj'} \\ &+ \sum_S S_x \sum_j (c^l_{Sj})^* c^m_{Sj} \,, \end{aligned} \tag{3}$$

where we have also neglected orbital overlap. Here S_x is the x-component of the coordinates of site S, and Δ_n denotes the site $S' = n$ in the local frame of S. Equation (3) has two types of local dipole transition moments. The first, on-site, term can take two possible values, one for Cd and

one for Se sites. The second term connects orbitals on different sites. We restrict n here to nearest neighbors, and the combination jj' to bonding interactions only, resulting in a single off-site transition moment between bonded nearest-neighbor Cd and Se atoms.

The incorporation of on-site and nearest-neighbor transition dipole moments introduces additional parameters beyond those needed to fit the energy band structure [65]. The three optical parameters defined above (on-site Cd, on-site Se and Cd-Se nearest-neighbor through-bond transition moments) were obtained by fitting to LDA density functional calculations of the bulk absorption spectra [69]. We found that the bulk absorption spectrum is relatively insensitive to the value of the on-site transition moments, reflecting the fact that the low energy range of the spectrum is dominated by transitions from the top of the valence band, which is primarily Se $4p$, into the bottom of the conduction band, which is primarily Cd $5s$, and therefore must be controlled by the nearest-neighbor transition moment between Cd and Se. Thus for simplicity we set $\langle j|\hat{x}|j'\rangle = 0$ in this work. The optimal value of the nearest-neighbor transition moment is then given by $\langle 0j|\hat{x}|\Delta_n j'\rangle = 1.8$ a.u.

3 Clusters with ideal, truncated surfaces: size and shape effects

Non-reconstructed truncated nanocrystals provide a reference point for the more realistic partially or completely capped surfaces, with and without reconstruction. Eigenenergies are calculated for wurtzite clusters consisting of 144, 384, 393 and 456 semiconductor atoms, constructed to correspond to typical C_{3v} nanocrystals seen in TEM images [53–55]. Using the bulk density of CdSe, we can provide an approximate size estimate from the relation

$$\rho \cdot \frac{4\pi r^3}{3} = n_{\mathrm{Cd}} m_{\mathrm{Cd}} + n_{\mathrm{Se}} m_{\mathrm{Se}}\,, \tag{4}$$

where n_i and m_i correspond to the number and mass of atoms of species i in the cluster, respectively. This yields sizes of 16.1 Å, 22.7 Å, 23.8 Å and 25.8 Å diameter for the above sequence. (These estimates differ by less than 10% from sizes derived from moment-of-inertia ratios as was done in reference [65].) The 144, 393 and 456 clusters are weakly prolate, with ellipticity $\mu = 0.048$–0.049, while the 384 cluster is strongly prolate, with $\mu = 0.26$.

It is useful to first compare the valence band and conduction band properties of a typical truncated cluster with those of the bulk semiconductor. Tight-binding calculations for bulk CdSe (without crystal field contributions) show that the top of the valence band consists mainly of Se p orbitals, with some Cd $4s$ and $4p$ contribution, while the bottom of the conduction band is formed by Cd $4s$ states [70]. We observe the same general behavior in the clusters. For $N = 393$, the valence band maximum is shifted from 0 eV to -0.42 eV as a result of quantum confinement. From the top of the valence band down to

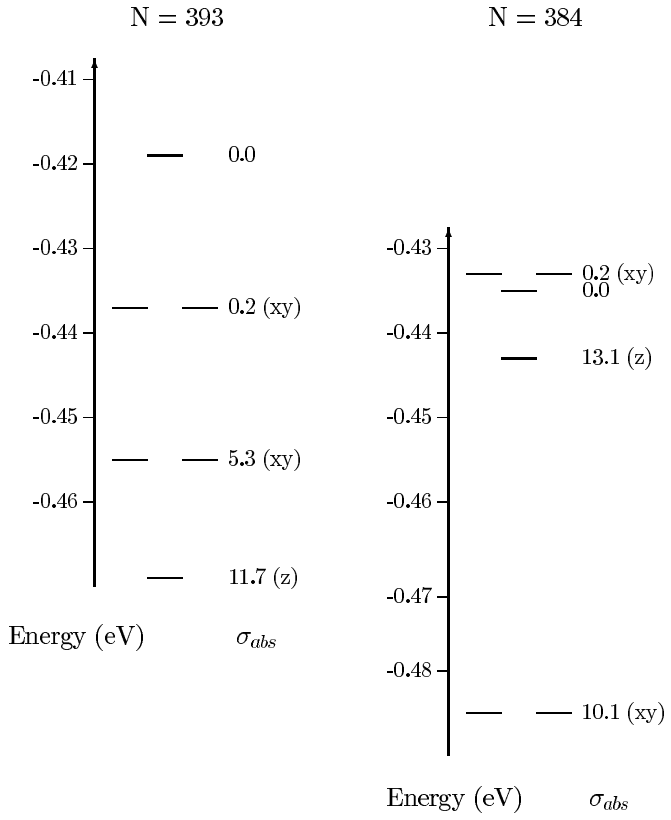

Fig. 5. Energy levels at the top of the valence band for $N = 393$ and 384 clusters with truncated surfaces. The column σ_{abs} lists the absorption coefficients for transitions from the valence band eigenstates into the conduction band, in arbitrary units. Letters in parentheses to the right of the numerical value denote the polarization of the transition.

energies of -2.2 eV, the p contributions constitute more than 95% of the total density of states. However, in contrast to the bulk where the valence band edge is dominated by the Se p contribution, the Cd p contribution forms a significant part (almost 30%) of the total p contribution in the valence band of the cluster. The bottom of the conduction band (located at 2.48 eV for $N = 393$) is almost entirely formed by Cd s states, with a 10% contribution from Se s states. At higher conduction band energies the Cd s percentage drops, falling to 50% at 3.28 eV, while the Cd p contribution increases rapidly. These size-dependent trends can be summarized by the general observation that the mixing of different orbital types increases with decreasing size.

The single-particle band gap energies can be extracted from the DOS by substracting the energy of the LUMO level from the energy of the HOMO level. To obtain an estimate of the exciton energy which can be compared to the experimentally measured position of the first excitonic peak in the absorption spectrum, we take the difference of the valence and conduction band states yielding the first strong absorption. Typically this is the third hole level from the band edge, as indicated in Figure 5 for $N = 393$ and 384. These are the first hole levels which are primarily interior in character: the valence band edge levels have

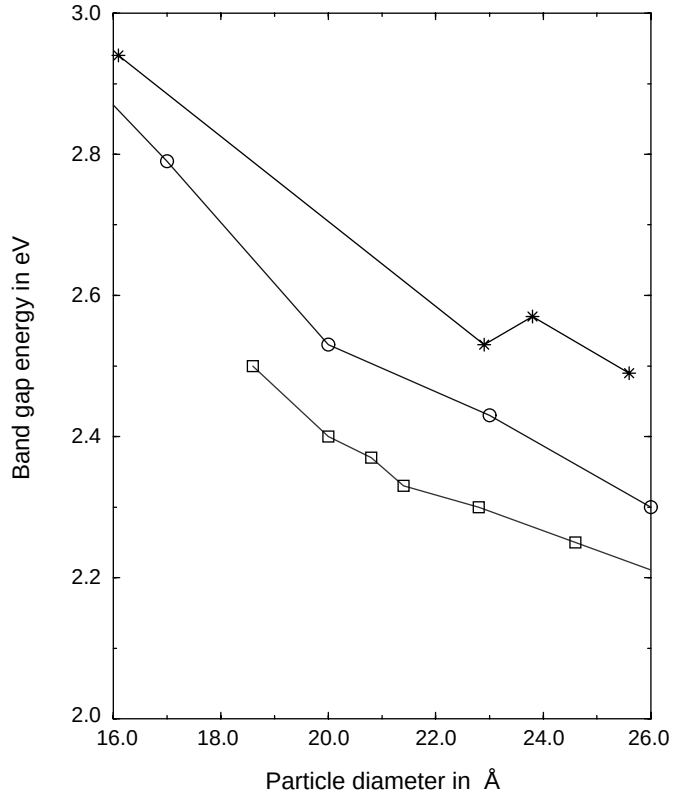

Fig. 6. Lowest excitonic energies for pure CdSe clusters with truncated surfaces. Stars (*) represent values calculated here, circles (◯) experimental values from reference [71] and squares (□) experimental values from reference [25].

a large surface contribution and are consequently generally only weakly absorbing. We refer to this absorption-defined gap as the "interior" gap. Correcting these "interior" band gap energies by the usual perturbative estimate of the electron-hole interaction [3,28] yields an estimate of the exciton energy which is compared to experimental values for this range of cluster sizes [25,71] in Figure 6. Allowing for the band gap increase due to surface truncation (this causes an artificial decrease in average coordination number, resulting in narrower bands and consequently in a larger band gap than a realistic, ligand-terminated surface), reasonable agreement with the available experimental data is obtained. (The spread in the latter is due to differences between sizings derived from small angle X-ray scattering and from transmission electron microscopy [25].) The slight decrease in the theoretical value on decreasing diameter from 23.8 Å ($N = 393$) to 22.7 Å ($N = 384$) is due to a change in the particle shape, as discussed below.

The shape of the nanocrystal provides an additional factor influencing the size dependence of single-particle electronic properties, modifying the level degeneracy and also the polarization of transition dipole moments. This is best understood by reference to bulk and to spherical clusters. When crystal field splitting terms are not explicitly included, as in the present calculations, the valence band edge levels of both bulk and spherical clusters correspond to those of cubic symmtry and are three-fold degenerate. In contrast, in nanocrystals with C_{3v} point group symmetry these triply degenerate levels are split into singly degenerate A and doubly degenerate E sets [53].

On varying the shape of the clusters from near spherical to strongly prolate, we see the effects of this shape-dependent splitting on both the DOS and the absorption spectra. This is illustrated by comparison of the electro-optic properties of the 393 and 384 clusters. The 384 cluster is created from the weakly prolate 393 cluster by removing nine atoms from the side faces of the 393 cluster (see Figs. 2a and 2b). This small change in total atom number gives rise to a large change in shape. The 384 cluster is considerably elongated relative to the 393 cluster, expressed quantitatively by a large change in ellipticity, from $\mu = 0.048$ to 0.26. These two clusters have significant electronic structure differences which would not be apparent from their very similar effective diameters (22.7 Å for $N = 384$, and 23.8 Å for $N = 393$).

First, as evident in Figure 6 and noted above, the band gap energy for 384 is actually smaller than that for 393, which is the opposite of what would be predicted from the quantum size effect for spherical clusters based on these effective diameters. This feature can be partially understood within the EMA, in terms of the perturbation provided by a prolate shape on the envelope function. When spin-orbit coupling is neglected, the lowest energy hole state for a spherical cluster within EMA (with the convention of negative hole energies) has S_1 symmetry [72], corresponding to a triply degenerate envelope function. The prolate shape causes this to split into A and E levels, with the singly degenerate A level corresponding to hole motion along the c-axis, and the doubly degenerate E level to motion in the plane perpendicular to this. In the absence of crystal field effects (which also influence the relative energetics of A and E levels, as discussed below), the A level would be predicted by EMA to be the lowest energy hole state (highest in absolute energy) and to become stabilized to an increasing extent as the cluster becomes more prolate. However, the conduction band edge state deriving primarily from Cd $5s$ orbitals is non-degenerate, and since in CdSe it has a lower effective mass, would be energetically less affected. The result is a decrease in band gap with increasing prolate character for a given effective size, consistent with the observed difference between $N = 384$ and $N = 393$.

While appealing, this EMA picture is nevertheless too simple, as is evident from consideration of the detailed valence band edge energy level structure shown in Figure 5. Only the second (lower absolute energy) A/E set of levels is clearly consistent with a division between z and xy character, with eigenvectors possessing $z : xy$ ratios of 1:100 or 100:1 for both levels. The first set of levels, A_1/E_1, have a large component of Cd p orbitals, in addition to Se orbitals, and also contain a larger surface component than the second set of levels, A_2/E_2, which can be regarded as primarily interior states. As a result of this orbital mixing, EMA arguments, which intrinsically assume a

factorization of atomic (Bloch) and envelope functions cannot be directly applied to the first set of levels.

Despite the more extreme polarization ratios for the second set of levels, these also do not follow the EMA predictions for prolate clusters. Thus, while there is a large downward hole shift (upward absolute energy shift) for A_2 on going from $N = 393$ to $N = 384$, for $N = 393$ E_2 is actually lower in absolute energy than A_2, in contradiction of the EMA prediction for a weak elliptical shape perturbation. This reflects a second marked difference between the $N = 393$ and 384 clusters, namely that the ordering of the A and E levels is reversed within both of the first two sets of valence band edge states (Figure 5). Consequently the polarization of the first transition with a large absorption coefficient will change from xy- to z-polarized when the cluster shape is changed from the slightly prolate 393 cluster (interband transition from E_2) to the more elongated 384 cluster (interband transition from A_2). Evidence for such a cross-over has been seen in resonance Raman depolarization measurements [53] and in ultra-fast absorption measurements [73]. Within EMA, crystal field effects can be invoked perturbatively to argue that in a spherical cluster with wurtzite structure the E levels will lie below A in absolute energy, and could therefore give rise to such a cross-over from E/A to A/E ordering as the ellipticity increases and as the envelope function for the A level is preferentially stabilized [53]. In EMA, the cross-over can thus be regarded as resulting from a competition between the effects of hexagonal lattice symmetry on the Bloch function, and of the nanocrystal shape on the envelope function. In tight-binding, despite the lack of factorization of Bloch and envelope functions for any finite nanocrystal, large ellipticity can still effect a stabilization of the energy level polarized primarily along the z-axis (A), because of the dominance of the delocalization differential between z- and xy-directions. However, since there is no crystal field effect explicitly incorporated here, the observed cross-over at weakly prolate shapes has to be due to a balance of this delocalization anisotropy against an intrinsic property of the discrete lattice associated with the C_{3v} symmetry of the finite nanocrystal. We suggest that this is an internal field produced by the uncompensated interactions in the z-direction resulting from the lack of mirror plane symmetry in the C_{3v} nanocrystals. This will preferentially lower the p_z orbitals in absolute energy just as the conventional crystal field does and so cause A_2 to lie below E_2 for weakly prolate crystals. Such an internal field will be present in any C_{3v} nanocrystal constructed from an atomistic model, regardless of the range of interactions. A corollary of such a shape-induced field is the presence of a non-zero dipole moment, which is consistent with recent dielectric dispersion measurements [48] and also with Stark measurements indicating a significant change in dipole moment upon absorption [44–46,74].

4 Nanocrystals capped with organic ligands

For clusters in the size range studied here, the organically capped surface has 60% of the Cd dangling orbitals satu-

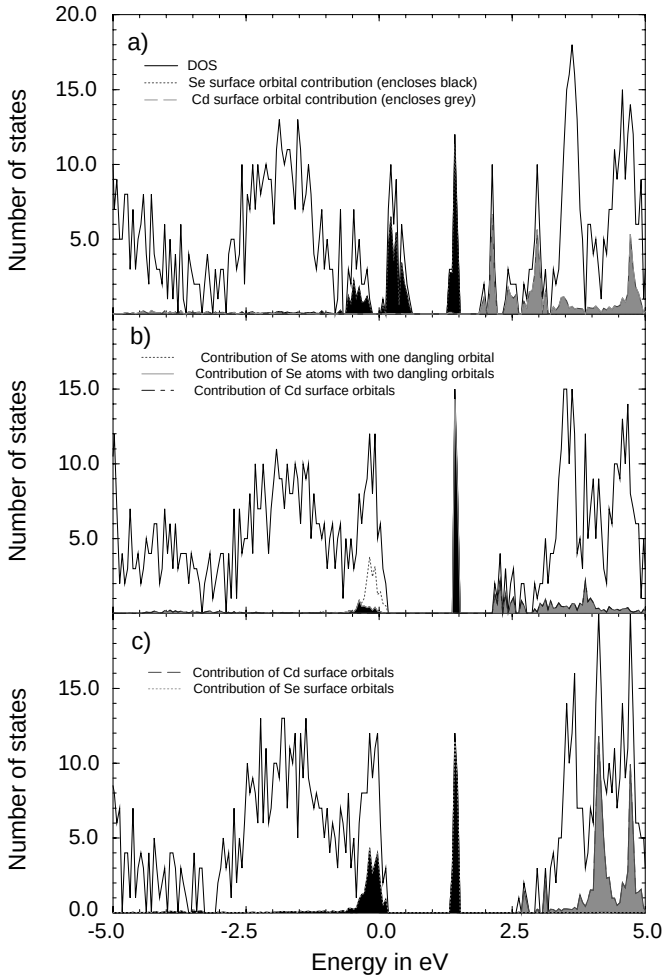

Fig. 7. DOS of the 393 cluster partially passivated by TOPO ligands, with various surface descriptions. (a) No reconstruction, sp_2 hybridized oxygen. (b) Reconstructed, sp_2 hybridized oxygen. (c) Reconstructed, sp_3 hybridized oxygen. Grey shaded areas denote Cd surface (dangling) orbital contributions. In (a) and (c), black areas denote all Se surface (dangling) orbital contributions, in (b) the black area denotes only contributions from Se atoms with two dangling orbitals.

rated by oxygen atoms representing TOPO, as described in Section 2. This corresponds to the measured TOPO surface coverage of a cluster of 393 semiconductor atoms ($\simeq$ 23 Å diameter) [25]. The large steric hindrance of bulky ligands like TOPO does not appear to allow for a higher surface coverage. For $N = 393$, this degree of coverage results in an additional 30 oxygen atoms attached to the cluster (Fig. 1a). (For ease of comparison with capped clusters, we continue to label clusters by the total number of semiconductor atoms only, *i.e.* ignoring the ligand atoms.)

In the first series of calculations, the oxygen is sp_2-hybridized, consistent with a weak σ donating bond to Cd. The DOS of the 393 cluster covered with oxygen with this hybridization is shown in Figure 7a. It shows important surface contributions from both Se and Cd dangling orbitals in the band gap region, although part of the Cd

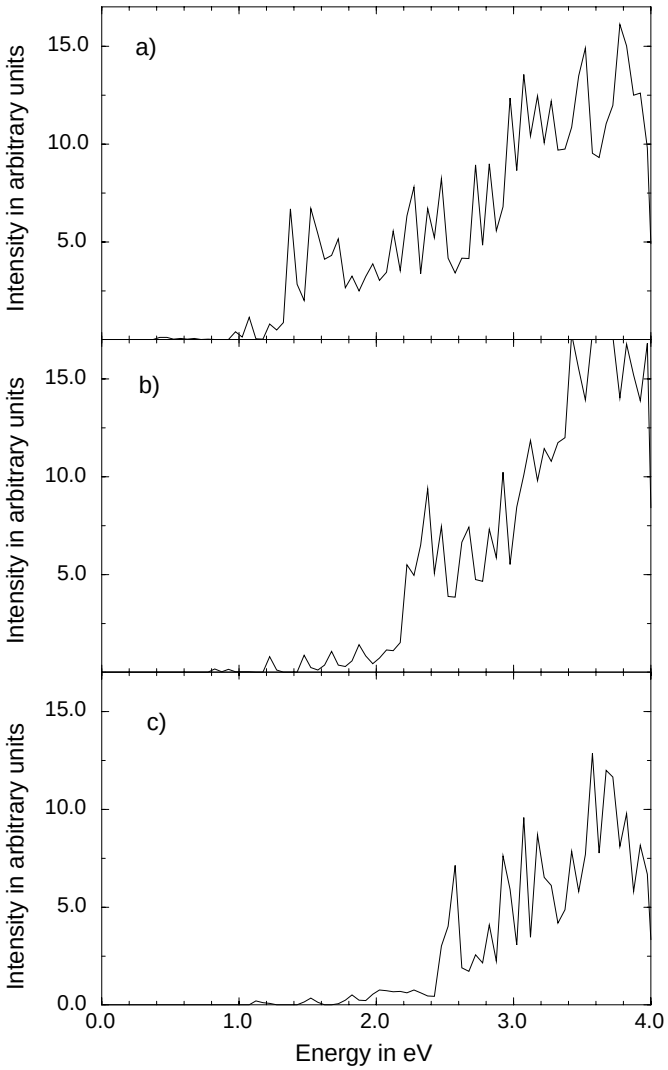

Fig. 8. Single-particle absorption spectra of the 393 cluster partially passivated by TOPO ligands, with various surface descriptions. (a) No reconstruction, sp_2 hybridized oxygen. (b) Reconstructed, sp_2 hybridized oxygen. (c) Reconstructed, sp_3 hybridized oxygen.

surface orbital density is shifted into the conduction band by the influence of the oxygen. In order to calculate the absorption spectrum, we need to determine the HOMO level. However this is not straightforward, because it is not clear how many electrons are donated into the cluster by the ligand. In the absence of experimental information on the extent of electron donation, we use the variations in calculated absorption spectra as a function of the HOMO position to estimate the optimal level. Comparison with experiment shows that a HOMO position of 1.47 eV, corresponding to donation of two electrons per ligand from 90% of the ligands, yields an optimal single-particle absorption spectrum. This is shown in Figure 8a. This assignment implies that the Se derived surface states are occupied with electrons (Fig. 7a), which is consistent with the large electronegativity of Se. Nevertheless, comparison of the resulting absorption spectrum in Figure 8a with the experimental spectrum shows that this idealized model of a capped cluster is still unrealistic, because strong absorption peaks arising from transitions between states with large surface contributions are visible in the energy range between 1.4 and 2.5 eV where no significant structure is observed in the experimental spectra [25].

4.1 Surface reconstruction

One possible reason for the discrepancy between calculated and experimental spectra seen with ideal surfaces is that the underlying assumption of a cluster surface with the structure of a bulk-terminated surface is not correct. This led us to consider reconstruction of the surface.

When considering the surface reconstruction of a faceted nanocrystal, it is useful to take the known bulk reconstructions of the facet surfaces as a guide. For CdSe, reconstructions of the (111) surface are well documented [57]. A tight-binding model of the bulk surface reconstruction for a clean (111) surface shows the main features to be movement of the Se surface atoms out of the surface plane, while the Cd surface atoms move in [57]. Straightforward application of this bulk result to our nanocrystals causes some difficulties however. Firstly, the C_{3v} clusters studied here do not have well defined single crystal surfaces. While some (111) facets can be identified, many atoms are located at edges or at highly stepped surface fragments. Furthermore, when the Cd dangling orbitals are saturated, the Cd atoms are much less likely to move inwards. To make a first, simple theoretical model for the reconstruction here, we therefore follow the model proposed by Bawendi *et al.* from fitting of X-ray structure data [50], in which it was assumed that the Se atoms move out along the bond direction by a distance of 1.0 Å while the Cd atoms are unaffected. This empirical estimate of the outward displacement of the Se atoms is a factor of 1.5 larger than the value calculated for the bulk (111) surface [57]. Although more complete calculations with full energy minimization [75] can be performed, this simple model is sufficient for a first analysis of the effects of reconstruction on the electronic properties.

The effect of this reconstruction on the density of states is shown in Figure 7b. The outward displacement of the surface Se atoms requires a rehybridization such that the *s*-contribution to the dangling Se orbitals increases. The resulting increase in energetically low-lying *s*-contributions shifts the energies of the Se surface states to lower values. Therefore we expect to see a shift of the Se surface states into the valence band. This is indeed observed for most of the Se density in the band gap region. However, as Figure 7b shows, this expected behavior is not observed for all Se surface states. One component of the Se dangling orbital states remains isolated in the middle of the band gap. These isolated, unshifted states are almost 100% assignable to surface states which are localized on Se atoms located on the cluster edges and which possess two dangling orbitals. The energies of these surface state lie approximately at one of the energies of an isolated Se

atom with two sp_3 orbitals. This suggests that the entire cluster provides only a weak perturbation on these atomic orbitals, so that the Se surface orbitals with two dangling bonds can be considered as effectively decoupled from the cluster. Consequently it is not surprising that they do not move much upon surface reconstruction. In contrast to this robust surface Se behavior, the Cd surface orbital density disappears almost completely out of the band gap region, with the main component of these states being shifted into the conduction band as a result of the saturation with oxygen. However, analysis of the absorption spectrum indicates that there is still some significant overlap between the valence band edge states and those states at the bottom of the conduction band which contain a high surface contribution of Cd orbitals. It is this overlap which is responsible for the unphysically large absorption peaks at very low transition energies apparent in Figure 8b.

4.2 Ligand hybridisation

The above calculations employed the native sp_2 hybridization of the oxygen in TOPO, implicitly assuming that the Cd-O interaction in the TOPO-cluster bond is weak. A stronger interaction leads in one extreme to sp_3 hybridized oxygen, as discussed in Section 2. The calculated absorption spectrum for a reconstructed cluster with all surface attached oxygen now being sp_3-hybridized is shown in Figure 8c. It is evident that there is now a complete shift of the Cd surface orbital densities into the conduction band density of states, and the resulting absorption spectrum shows no unphysical peaks at low energies. All important absorption peaks now lie in an energy range which would give the correct two-particle energies when corrected by perturbative excitonic effects [3,28]. Thus the stronger ligand-nanocrystal bond implicit in the sp_3 hybridization appears to provide a more realistic description for TOPO capped CdSe nanocrystals.

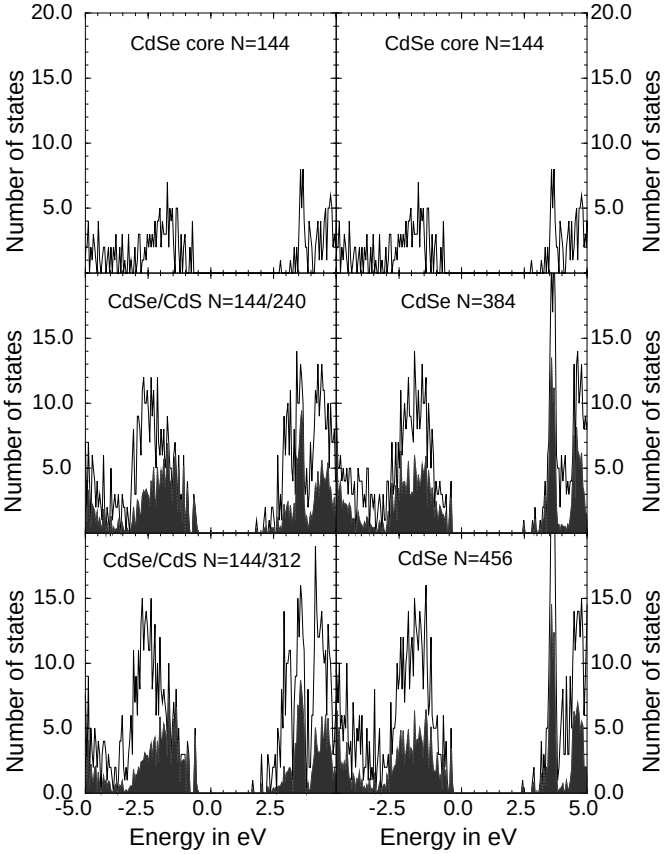

Fig. 9. DOS for CdSe/CdS core/shell nanocrystals. From top to bottom: pure CdSe core containing 144 atoms, core/shell cluster with 144 atom core and 240 atom shell (total of 384 semiconductor atoms), core/shell cluster with 144 atom core and 312 atom shell (total of 456 semiconductor atoms). Left-hand panels show the DOS of the CdSe/CdS core/shell particles, with shading indicating the CdSe core contribution. Right-hand panels show the DOS of pure CdSe clusters containing the same total number of semiconductor atoms. For comparison, the contribution from the core region is also shaded for the pure clusters.

5 Electronic structure of clusters capped with inorganic shells

Recently a new type of surface termination has been explored experimentally, namely the saturation of the dangling bonds by another semiconductor material [76–80]. Here one or more layers of a second semiconductor are grown epitaxially on the nanocrystal, leading to the formation of a shell of second semiconductor surrounding a core of the first material. Such core/shell particles offer the possibility of complete passivation of both anionic and cationic surface sites, in contrast to the capping by organic ligands discussed above, where ligand polarity and steric hindrance restrict the extent of surface passivation. This suggests that surface defects and traps can be efficiently eliminated by inorganic epitaxial growth. In addition, when several layers are grown, *i.e.*, so that a true shell rather than an inorganic ligand is providing the capping, the core/shell nanoparticle constitutes the zero-dimensional analogue of a two-dimensional semiconductor heterostructure. This offers additional control over the spatial localization of electron and hole, by making use of band gap offsets to preferentially localize one or both carriers in one of the two components (Sect. 2).

In this section we investigate the effect of such an inorganic shell on the electronic properties of CdSe nanocrystals, by adding several layers of CdS to a CdSe core cluster containing 144 atoms (∼16.1 Å diameter). Addition of two layers results in a cluster with a total number of 384 (∼22.7 Å diameter) semiconductor atoms, while three layers results in 456 semiconductor atoms (∼25.8 Å diameter). As outlined in Section 2, stress and strain are neglected at the interface. The construction of tight-binding parameters providing a consistent framework for the band off-sets in the bulk heterostructures was described in Section 2. The outer shell surface is truncated, which is

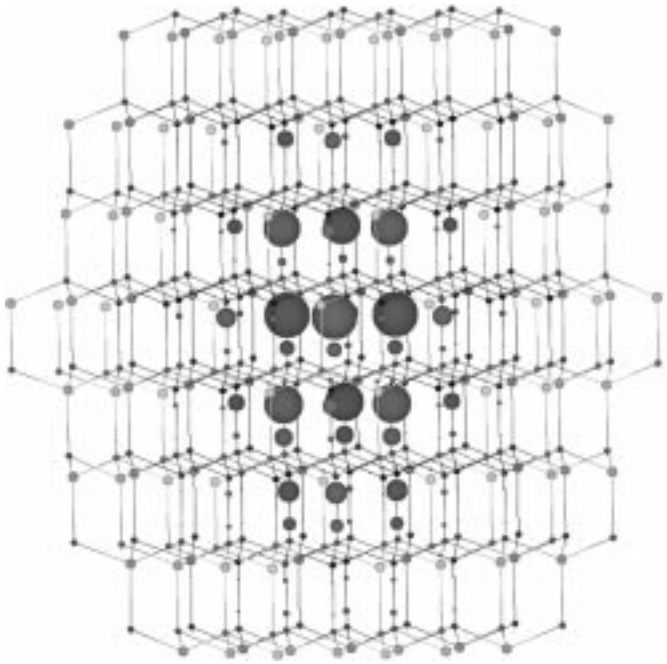

Fig. 10. Hole density distribution in the valence band edge eigenstate of the 384 atom core/shell cluster. The hole density, represented by large grey spheres of radius proportional to the density on a particular site, is concentrated in the CdSe core. Sulfur is represented by light grey spheres, while Cd and Se are represented by black spheres.

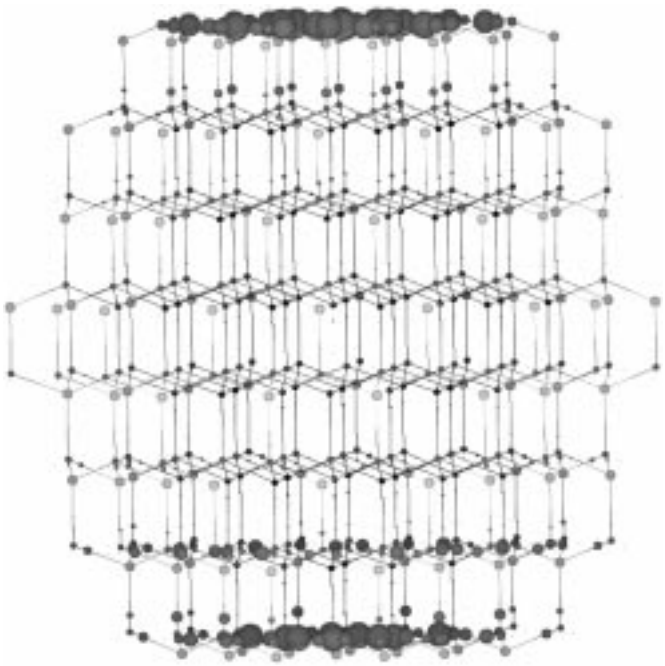

Fig. 11. Electron density distribution in the conduction band edge eigenstate of the core/shell cluster with 384 semiconductor atoms. The electron density, represented by large black spheres proportional to the density on a particular site, is concentrated in the CdS shell.

justified by the observed large photo-luminescence quantum yield and lack of deep trap emission [78,79]. These indicate that dangling orbitals on the shell are not important for the electronic properties of these core/shell systems, provided that the shell is thick enough.

Figure 9 shows on the left the DOS for two sizes of core/shell particles and compares them with the corresponding DOS of pure CdSe nanocrystals on the right. Both particles have a CdSe core with 144 atoms. The DOS of the bare core is shown in the top panel for reference, and is therefore identical for left and right. The middle panel refers to a core/shell particle with total number of atoms equal to 384, and the bottom panel to a core/shell particle with 456 atoms in total. Thus the relative thickness of the shell is increasing from top to bottom. For the pure clusters the contribution from the core region is also shown shaded, for ease of comparison. The valence band edge of the mixed clusters is clearly dominated by the CdSe core. $N = 384$ has 90% core contribution to these states. In contrast, the conduction band edge states are dominated by the CdS shell, with only about 25% core contribution. After normalizing by the number of core and shell atoms, we find that for both the 384 and the 456 cluster, the hole density in the core region for the valence band edge states is about three times larger than the average hole density (Fig. 10). In the shell region however, the hole density is only one quarter of the average density. At the conduction band edge the opposite behavior is found, although the contrasts are less extreme. Thus the electron density in the core is about 25% of its average density, while in the shell region it is about 20% higher than the average electron density (Fig. 11). Higher energy eigenstates in the conduction band show a decreasing core contribution, until at about 2.9 eV a sharp rise in the core contribution to average electron density occurs. For even higher energies the core contributions to the electron density decrease once again.

These results imply that within the single-particle approximation to the excited electron-hole pair state, the hole is primarily confined in the core, while the electron is more evenly (but not uniformly) distributed over both core and shell. This would result in a lower confinement energy for the electron upon coating with the CdS shell, and is consistent with the experimentally observed red shifts of the first excitonic absorption with increasing shell thickness [78,80]. Explicit calculation of the absorption spectra for these particles will require careful consideration of the transition dipole moments at the interface and is not made here.

For CdSe/CdS the band edge electron and hole densities derived from tight-binding generally confirm the qualitative predictions of the simple particle-in-a-box model used by Peng *et al.* [78]. The greatest difference from the simple picture is found in the electron density, which is much more inhomogeneous in the tight-binding calculations. Our calculations show that the electron density in the shell region is about six times greater than in the core region, for states at the conduction band edge. This may be due in part to the opposite sign of conduction band off-set assumed in the model of reference [78] which

resulted in a type-I bulk interface and which would raise the relative electron density in the core region. Nevertheless, the tight-binding results show that there is still a sizeable probability for the electron to remain in the core region.

Our primary conclusion is therefore that the 0D CdSe/CDs heterostructure is not as "spatially indirect" as its 2D bulk analog. Because of the penetration of the hole to shell regions (10%) and of electron to the core regions (25%), it is neither possible to conclude that the electron/hole spectral overlap is dominated by one or other spatial region (type I), nor that it is localized at the interface (type II). The band edge states are differentially localized, but are not clearly separated. Similar behavior is seen in the CdSe/ZnS core/shell nanocrystals, for which the bulk band offsets are even greater [80], and for which greater charge separation would be expected. Consequently the classification into either type I, "spatially direct" or type II, "spatially indirect" interfaces appears to not be meaningful for 0D heterostructures. The similarity of results reached from tight-binding with results from particle-in-a-box calculations [78,80] suggests that the reduced charge separation in the core/shell nanocrystals is quite general and due to the curvature of the interface.

6 Conclusions

By changing the shape of clusters with truncated surfaces, we have shown that electronic and optic properties can be strongly dependent on nanocrystal shape, as well as on size. This has important consequences for analysis of experimental spectra, since in most experimental procedures for generating clusters it is possible to control the average size but not the shape. This sensitivity of the electronic properties to cluster shape accounts for some of the difficulties in quantitatively matching theoretical and experimental results by consideration of only the size dependence.

Upon adding oxygen ligands and dangling orbitals to model the surface of CdSe nanocrystals partially passivated by TOPO, we find that absorption spectra giving reasonable agreement with experimental data can be calculated only after allowing for: i) reconstruction of the surface, and ii) formation of a stronger bond with the oxygen ligands than would be predicted by the native sp_2 hybridization of oxygen in TOPO. The results of the relatively simple model of a surface reconstruction employed here leads us to conclude that reconstruction of the surface can indeed have a major effect on the electronic and optical properties. More detailed studies of surface reconstruction will be presented elsewhere [65].

When the surface of a CdSe nanocrystal is saturated with shells of inorganic species (CdS) to create core/shell particles (0D heterostructures) we find that this causes a differential localization of the valence and conduction band edge states. This differential localization is qualitatively different from that seen in bulk 2D heterostructures, with neither complete spatial overlap nor clean spatial separation of electron and hole. This suggests more generally that the classification of heterojunctions as "spatially indirect", type II, or "spatially direct", type I, is rendered inaccurate for spatially curved interfaces. This deserves more general study. In this particular case, the valence band states are dominated by CdSe core contributions, while the conduction band edge states are more evenly distributed over core and shell, but possessing somewhat greater weight in the CdS shell. This has consequences for the efficiency of overlap in the excited state, and introduces an additional control variable for the optical properties of artificially engineered core/shell particles. More detailed theoretical calculations on these confined heterostructures would be of great interest.

This work was supported by a grant from Sandia National Laboratories, Contract Number AR-9600, and by the Materials Design Initiative at Lawrence Berkeley Laboratory under ONR Contract N0001495F0099. KBW thanks the A. Von Humboldt Foundation for a Senior Research Award, and SP thanks the Studienstiftung des Deutschen Volkes for a Diplom Fellowship. Computational work was performed at the San Diego Supercomputer Center on the C90.

References

1. A.P. Alivisatos, Science **271**, 933 (1996).
2. Al.L. Efros, A.L. Efros, Sov. Phys. Semicond. **16**, 772 (1982).
3. L.E. Brus, J. Chem. Phys. **80**, 4403 (1984).
4. N. Chestnoy, R. Hull, L.E. Brus, J. Chem. Phys. **85**, 2237 (1986).
5. See, *e.g.*, H. Haug, S.W. Koch, *Quantum Theory of the Optical and Electronic Properties of Semiconductors* (World Scientific, Singapore, 1993).
6. A.I. Ekimov, F. Hache, M.C. Schanne-Klein, D. Ricard, C. Flytzanis, I.A. Kudryavtsev, T.V. Yazeva, A.V. Rodina, Al.L. Efros, J. Opt. Soc. Am. (B) **10**, 100 (1993).
7. Al.L. Efros, M. Rosen, M. Kuno, M. Nirmal, D.J. Norris, M.G. Bawendi, Phys. Rev. B **54** , 4843 (1996).
8. M.L. Steigerwald, L. E. Brus, Acc. Chem. Res. **23**, 183 (1990).
9. M.G. Bawendi, P.J. Carroll, W.L. Wilson, L.E. Brus, J. Chem. Phys. **96**, 946 (1992).
10. W. Hoheisel, V.L. Colvin, C.S. Johnson, A.P. Alivisatos, J. Chem. Phys. **101**, 8455 (1994).
11. D. Mittleman, S.J. Rosenthal, R.W. Schoenlien, A.T. Yeh, J.J. Shiang, V.L. Colvin, R.A. Grubbs, A.P. Alivisatos, C.V. Shank, Springer Ser. Chem. Phys. **60**, 351 (1994).
12. T.W. Roberti, N.J. Cherepy, J.Z. Zhang, J. Chem. Phys. **108**, 2143 (1998).
13. M. Kuno, J.K. Lee, B.O. Dabbousi, F.V. Mikulec, M.G. Bawendi, J. Chem. Phys. **106**, 9869 (1997).
14. M. O'Neil, J. Marohn, and G. McLendon, J. Phys. Chem. **94**, 4356 (1990).
15. A. Eychmueller, A. Haesselbarth, L. Katsikas, H. Weller, Ber. Bunsenges. Phys. Chem. **95**, 79 (1991).
16. A. Haesselbarth, A. Eychmueller, H. Weller, Chem. Phys. Lett. **203**, 271 (1993).
17. M. Nirmal, C.B. Murray, D.J. Norris, M.G. Bawendi, Z. Phys. D **26**, 361 (1993).

18. M. Nirmal, C.B. Murray, M.G. Bawendi, Phys. Rev. B **50**, 2293 (1994).
19. D.B. Tran Thoai, Y.Z. Hu, S.W. Koch, Phys. Rev. B **42**, 11261 (1990).
20. P. Lippens, M. Lannoo, Phys. Rev. B **39**, 10935 (1989).
21. P. Lippens, M. Lannoo, Phys. Rev. B **41**, 6079 (1990).
22. N.A. Hill, K.B. Whaley, J. Chem. Phys. **99**, 3707 (1993).
23. N.A. Hill, K.B. Whaley, J. Chem. Phys. **100**, 2831 (1994).
24. L.R. Becerra, C.B. Murray, R.G. Griffin, M.G. Bawendi, J. Chem. Phys. **100**, 3297 (1994).
25. J.E. Bowen Katari, V.L. Colvin, A.P. Alivisatos, J. Phys. Chem. **98**, 4109 (1994).
26. A.C. Carter, C.E. Bouldin, K.M. Kemmer, M.I. Bell, J.C. Woicik, S.A. Majetich, Phys. Rev. B **55**, 13822 (1997).
27. N.A. Hill, K.B. Whaley, J. Electron. Mater. **25**, 269 (1996).
28. N.A. Hill, K.B. Whaley, Chem. Phys. **210**, 117 (1996).
29. S.V. Nair, L.M. Ramaniah, K.C. Rustagi, Phys. Rev. B **45**, 5969 (1992).
30. L.M. Ramaniah, S.V. Nair, Phys. Rev. B **47**, 7132 (1993).
31. R.S. Kane, R.E. Cohen, R. Silbey, J. Phys. Chem. **100**, 7928 (1996).
32. H.H. Von Gruenberg, Phys. Rev. B **55**, 2293 (1997).
33. L.-W. Wang, A. Zunger, J. Phys. Chem. **98**, 2158 (1994).
34. L.-W. Wang, A. Zunger, Phys. Rev. B **53**, 9579 (1996).
35. T. Uda, M. Hirao, J. Phys. Soc. **63**, Suppl. B, 97 (1994).
36. B. Delley, E.F. Steigmeier, Phys. Rev. B **47**, 1397 (1993).
37. K. Eichkorn, R. Ahlrichs, Chem. Phys. Lett. **288**, 235 (1998).
38. D.J. Norris, A. Sacra, C.B. Murray, M.G. Bawendi, Phys. Rev. Lett. **72**, 2612 (1994).
39. D.J. Norris, M.G. Bawendi, J. Chem. Phys. **103**, 5260 (1995).
40. A. Sacra, D.J. Norris, C.B. Murray, M.G. Bawendi, J. Chem. Phys. **103**, 5236 (1995).
41. D.J. Norris, M.G. Bawendi, Phys. Rev. B **53**, 16338 (1995).
42. M. Nirmal, B.O. Dabbousi, M.G. Bawendi, J.J. Jacklin, J.K. Trautman, T.D. Harris, L.E. Brus, Nature **383**, 802 (1996).
43. M. Kuno, M. Nirmal, M.G. Bawendi, A. Efros, M. Rosen, J. Chem. Phys. **108**, 4242 (1998).
44. V.L. Colvin, A.P. Alivisatos, J. Chem. Phys. **97**, 730 (1992).
45. V.L. Colvin, K.L. Cunningham, A.P. Alivisatos, J. Chem. Phys. **101**, 7122 (1994).
46. S.P. Empedocles, M.G. Bawendi, Science **278**, 2114 (1997).
47. D. Mittleman, R.W. Schoenlien, J.J. Shiang, V.L. Colvin, A.P. Alivisatos, C.V. Shank, Phys. Rev. B **49**, 14435 (1994).
48. S.A. Blanton, A. Dehestani, P.C. Lin, P. Guyot- Sionnest, Chem. Phys. Lett. **229**, 317 (1994).
49. S.A. Blanton, M.A. Hines, M.E. Schmidt, P. Guyot-Sionnest, J. Lumin. **70**, 254 (1996).
50. M.G. Bawendi, A.R. Kortan, M.L. Steigerwald, L.E.Brus, J. Chem. Phys. **91**, 7282 (1989).
51. S.H. Tolbert, A.P. Alivisatos, J. Chem. Phys. **102**, 4642 (1995).
52. S.A. Blanton, R.L. Leheny, M.A. Hines, P. Guyot-Sionnest, Phys. Rev. Lett. **79**, 865 (1997).
53. J.J. Shiang, A.V. Kadavanich, R.K. Grubbs, A.P. Alivisatos, J. Phys. Chem. **99**, 17417 (1995).
54. A.V. Kadavanich, A. Mews, S.H. Tolbert, X. Peng, M.C. Schlamp, J.C. Lee, A.P. Alivisatos, MRS Symposium Proceedings 452 (MRS, Pittsburgh, 1997) p. 353.
55. A.V. Kadavanich, Ph.D. Thesis, University of California, Berkeley, 1997.
56. Al.L. Efros, Phys. Rev. B **46**, 7448 (1992).
57. Y. Wang, C. Duke, Phys. Rev. B **37**, 6417 (1988).
58. P. Vogl, H.P. Hjalmarson, J.D. Dow, J. Phys. Chem. Sol. **44**, 365 (1981).
59. J.C. Slater, G.F. Koster, Phys. Rev. B **94**, 1498 (1954).
60. See *e.g.*, M.L. Cohen, J.R. Chelikowsky, *Electronic Structure and Optical Properties of Semiconductors* (Springer Verlag, New York, 1989) p. 149.
61. F.A. Cotton, R.D. Barnes, E.J. Bannister, J. Chem. Soc., 2199 (1960).
62. N. Burford, B.W. Royan, R.E.v.H. Spence, T.S. Cameron, A. Linden, R.D. Rogers, J. Chem. Soc. Dalton Trans., 1521 (1990).
63. F.R. Hartley, *The Chemistry of Organophosphorus Compounds*, vol. 2 (Wiley, New York, 1992).
64. J.P. Rose, R.A. Lalancette, J.A. Potenza, H.J. Schugar, Acta Cryst. B **36**, 2409 (1980).
65. K. Leung, S. Pokrant, K.B. Whaley, Phys. Rev. B **57**, 12291 (1998).
66. M.P. Halsall, J.E. Nicholls, J.J. Davies, B. Cockayne, P.J. Wright, A.G. Cullis, Semicond. Sci. Technol. **3**, 1126 (1988).
67. W. Langbein, M. Heffereich, M. Gruen, C. Klingshirn, H. Kalt, Appl. Phys. Lett. **65**, 2466 (1994).
68. W.A. Harrison, *Electronic Structures and the Properties of Solids* (W. H. Freeman, New York, 1980) p. 253.
69. Z. Xu, Solid State. Commun. **76**, 1143 (1990).
70. A. Kobayashi, O. Sankey, S. Volz, J. Dow, Phys. Rev. B **28**, 935 (1983).
71. C.B. Murray, M. Nirmal, D.J. Norris, M.G. Bawendi, Z. Phys. D **26**, S231 91993).
72. J.-B. Xia, J. Lumin. **70** 120 (1996).
73. S.J. Rosenthal, A.T. Yeh, A.P. Alivisatos, C.V. Shank, Springer Ser. Chem. Phys. **60**, 351 (1996).
74. M.E. Schmidt, S.A. Blanton, M.A. Hines, P. Guyot-Sionnest, J. Chem. Phys. **106**, 5254 (1997).
75. K. Leung, K.B. Whaley, J. Chem. Phys. in press (1999).
76. D. Schoss, A. Mews, A. Eychmüller, H. Weller, Phys. Rev. B **49**, 17072 (1994).
77. Y. Tian, T. Newton, N.A. Kotov, D.M. Guldi, J.H. Fendler, J. Phys. Chem. **100**, 8927 (1996).
78. X. Peng, M.C. Schlamp, A.V. Kadavanich, A.P. Alivisatos, J. Am. Chem. Soc. **119**, 7019 (1997).
79. M. Kuno, J.K. Lee, B.O. Dabbousi, F.V. Mikulec, M.G. Bawendi, J. Chem. Phys. **106**, 9869 (1997).
80. B.O. Dabbousi, R. Rodriguez-Viejo, F.V. Mikulec, J.R. Heine, H. Mattoussi, R. Ober, K.F. Jensen, M.G. Bawendi, J. Phys. Chem. B **101**, 9463 (1997).